J. Fluid Mech. (2011), *vol.* 671, *pp.* 574–586.
doi:10.1017/S0022112010006075

The action of waving cylindrical rings in a viscous fluid

HOA NGUYEN, RICARDO ORTIZ, RICARDO CORTEZ AND LISA FAUCI†

Department of Mathematics and Center for Computational Science, Tulane University, New Orleans, LA 70118, USA

(Received 12 September 2010; revised 16 November 2010; accepted 17 November 2010)

Dinoflagellates (*Pfisteria piscicida*) are unicellular micro-organisms that swim due to the action of two eucaryotic flagella: a trailing, longitudinal flagellum that propagates planar waves and a transverse flagellum that propagates helical waves. Motivated by the wish to understand the role of the transverse flagellum in dinoflagellate motility, we study the fundamental fluid dynamics of a waving cylindrical tube wrapped into a closed helix. Given an imposed travelling wave on the structure, we determine that the helical ring propels itself in the direction normal to the plane of the circular axis of the helix. The magnitude of this translational velocity is proportional to the square of the helix amplitude. Additionally, the helical ring exhibits rotational motion tangential to its axis. These calculated swimming velocities are consistent when using the method of regularized Stokeslets with prescribed wave kinematics, regularized Stokeslets with dynamic forcing and Lighthill's slender-body theory, except in cases where the slenderness parameter is not small. The translational velocity results are nearly indistinguishable using the three approaches, leading to the conjecture that the main contribution to this velocity at a cross-section is the far-field flow generated by the portion on the opposite side of the ring. The largest contribution to the rotational velocity at a cross-section comes from the cross-section itself and others nearby, thus the geometric details of the slender body have a larger effect on the results.

Key words: micro-organism dynamics, slender-body theory, swimming/flying

1. Introduction

Dinoflagellates (*Pfisteria piscicida*) are unicellular micro-organisms that are an important part of the aquatic food chain. Algal blooms of a certain dinoflagellate species give rise to 'red tides' and bioluminescent dinoflagellates light up some marine bays (Latz *et al.* 2008). Dinoflagellates swim due to the action of two eucaryotic flagella – a trailing, longitudinal flagellum that propagates planar waves and a transverse flagellum that propagates helical waves (see figure 1). The swimming trajectories of these cells are helical (Sheng *et al.* 2007), and each cell exhibits both rotation about its longitudinal axis and translation along the same axis. The transverse flagellum wraps around the cell like a belt in a plane perpendicular to the trailing flagellum. An interesting aspect of the swimming motion of dinoflagellates is that

† Email address for correspondence: ljf@math.tulane.edu

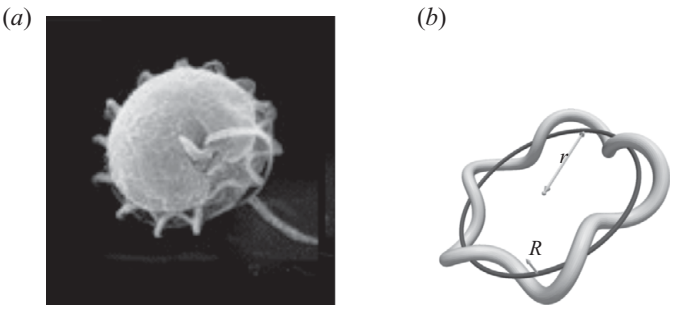

FIGURE 1. (*a*) A micrograph of the dinoflagellate, *Pfisteria piscicida* (courtesy of the Aquatic Botany Lab, NC State, USA). (*b*) A cylindrical ring that is helically wrapped around a baseline circle of radius r. The amplitude of the helix is R.

there is no consensus in the literature about the principal roles of the two flagella. The transverse flagellum had been thought to be responsible for the cell's rotation, whereas the longitudinal flagellum was thought to induce forward motion of the cell (Gaines & Taylor 1985; Cachon *et al.* 1991; Fenchel 2001). Fenchel (2001) writes 'In principle, the transversal flagellum should then only generate a net torque in a direction perpendicular to the longitudinal axis of the cell'. However, it was observed that when some cells lacked a longitudinal flagellum, they still exhibited forward motion (Cachon *et al.* 1991). More recently, Miyasaka *et al.* (2004) used resistive force theory to examine the functional role of the flagella of *Prorocentrum minimum*, and asserted that 'The transverse flagellum works as a propelling device that provides the main driving force or thrust to move the cell along the longitudinal axis of its helical swimming path'.

Motivated by the classical work by Taylor (1952), who examined the swimming of a waving cylindrical tail in a Stokes fluid, we isolate the function of the dinoflagellate transverse flagellum by addressing the simplified scenario of a helical tube wrapped into a closed ring. We ask the question: if a travelling wave is imposed on the closed helical ring, what propulsion does it generate? Our goal is to determine the fundamental fluid dynamics of a waving cylindrical ring in a Stokes fluid using various numerical approaches. For instantaneous fluid velocities generated by an imposed travelling wave on the structure, we use the slender-body theory of Lighthill (1976). Alternatively, we use the method of regularized Stokeslets (Cortez 2001; Cortez, Fauci & Medovikov 2005) to compute the instantaneous swimming velocities. Our results show that the ring exhibits both rotational motion and translational progression in the direction perpendicular to the plane of the ring.

A dynamic model of the helical ring is also presented by constructing the elastic tube from nodes connected by springs whose forces are generated by time-varying resting lengths. The resting lengths as functions of time come from the idealized helical ring with a travelling wave passing through it. The nodes move with the fluid velocity at their locations, which is computed with the method of regularized Stokeslets. The simplified flagellum ring model is interesting on its own and sheds light on the mechanics of dinoflagellate motility, even if the model does not include all components of the organism. The results also provide a test problem used to validate the use of regularized Stokeslets in the dynamic, elastic computations.

2. Mathematical model

The idealized flagellum centreline Γ is the closed circular helix described by

$$\left.\begin{aligned} X(s,t) &= \left[r - R\sin\left(\frac{2\pi s}{\lambda} - \omega t\right)\right]\cos\left(\frac{s}{r}\right), \\ Y(s,t) &= \left[r - R\sin\left(\frac{2\pi s}{\lambda} - \omega t\right)\right]\sin\left(\frac{s}{r}\right), \\ Z(s,t) &= R\cos\left(\frac{2\pi s}{\lambda} - \omega t\right), \end{aligned}\right\} \tag{2.1}$$

where $0 \leqslant s \leqslant 2\pi r = L$. The axis of this circular helix is a baseline circle of radius r in the plane $z = 0$. The helical amplitude is R and λ is the wavelength. The surface of the helical ring is then formed by circular cross-sections of radius r_h placed normal to the above centreline. Figure 1(b) depicts the thick helical ring along with the baseline circle around which the ring is wrapped. As time t progresses, a wave with speed $w_s = \omega\lambda/2\pi$ is imposed to travel around the ring. Without the fluid, a point on the centreline would trace a circle of radius R. The temporal period of the wave is $T = 2\pi/\omega$. Our goal is to determine how the imposed undulatory wave around the ring generates overall swimming of the ring in an unbounded, three-dimensional fluid.

We describe the fluid dynamics by the incompressible Stokes equations:

$$\mu\Delta\boldsymbol{u} = \nabla p - \boldsymbol{F}, \tag{2.2}$$

$$\nabla\cdot\boldsymbol{u} = \boldsymbol{0}. \tag{2.3}$$

Here, $\boldsymbol{u}$ is fluid velocity, p denotes pressure and μ is dynamic viscosity. The force of the undulating ring on the surrounding fluid is given by $\boldsymbol{F}$.

Dimensionless formulation. Choosing any characteristic scales for length ℓ and velocity U, we define dimensionless position $x' = x/\ell$, $\boldsymbol{u}' = \boldsymbol{u}/U$, time $t' = t(U/\ell)$, pressure $p' = p(\ell/\mu U)$ and force $\boldsymbol{F}' = \boldsymbol{F}(\ell^2/\mu U)$. This gives

$$\Delta\boldsymbol{u}' = \nabla p' - \boldsymbol{F}', \quad \nabla\cdot\boldsymbol{u}' = 0, \tag{2.4}$$

independent of the choice of ℓ and U. We choose these based on the flagellum parameters. Natural scales are $\ell = 2r$, the diameter of the baseline circle, and $U = \ell\omega/2\pi$ (so that the time scale becomes the period $T = \ell/U = 2\pi/\omega$).

On the basis of these definitions, we set $s' = s/\ell$, $R' = R/\ell$ and $\lambda' = \lambda/\ell$ to get the dimensionless flagellum centreline

$$\left.\begin{aligned} X'(s',t') &= \left[1/2 - R'\sin\left(\frac{2\pi s'}{\lambda'} - 2\pi t'\right)\right]\cos(2s'), \\ Y'(s',t') &= \left[1/2 - R'\sin\left(\frac{2\pi s'}{\lambda'} - 2\pi t'\right)\right]\sin(2s'), \\ Z'(s',t') &= R'\cos\left(\frac{2\pi s}{\lambda} - 2\pi t'\right), \end{aligned}\right\} \tag{2.5}$$

so that the dimensionless wave speed is $w_s' = \lambda'$. We also define $n_p = \pi/\lambda'$ as the integral number of pitches around the ring. For the remainder of the paper, we use the dimensionless formulation of the problem and drop the primes on the variables.

We point out that when using slender-body theory (Lighthill 1976), these forces are supported only along the one-dimensional centreline Γ of the helical ring (see

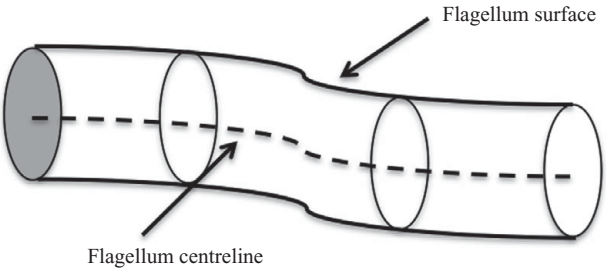

FIGURE 2. A schematic diagram of a section of the helical ring depicting its one-dimensional centreline Γ and surface Σ.

figure 2); however, when using regularized Stokeslets (Cortez 2001; Cortez, Fauci & Medovikov 2005), the forces are distributed on the surface Σ of the helical ring. In either case, the Stokes equations imply that the distribution of forces is linearly related to the distribution of velocities.

2.1. *Instantaneous fluid velocity computations*

In the static computations of instantaneous flows, we begin with an equation that encodes the linear relationship between the fluid velocity and the forces exerted by the flagellum. Generically,

$$\boldsymbol{u}(\boldsymbol{x}) = \mathscr{L}(\boldsymbol{x})[\boldsymbol{f}] \tag{2.6}$$

represents a slender-body theory, the regularized Stokeslet, or some other formulation where $\boldsymbol{f}$ represents a force density on the flagellum. Assuming the velocity distribution on the helical ring implied by (2.5), we must compute the distribution $\boldsymbol{f}$. However, for instantaneous computations of the ring velocity, we ensure conservation of linear and angular momentum by imposing

$$\int_\Gamma \boldsymbol{f}(\boldsymbol{X}(s))\,\mathrm{d}s = 0 \quad \text{and} \quad \int_\Gamma \boldsymbol{X}(s) \times \boldsymbol{f}(\boldsymbol{X}(s))\,\mathrm{d}s(\boldsymbol{x}) = 0 \tag{2.7}$$

in the case of slender-body theory, where the forces are concentrated along Γ, or

$$\iint_\Sigma \boldsymbol{f}(\boldsymbol{X}(\alpha,\beta))\,\mathrm{d}\alpha\,\mathrm{d}\beta = 0 \quad \text{and} \quad \iint_\Sigma \boldsymbol{X}(\alpha,\beta) \times \boldsymbol{f}(\boldsymbol{X}(\alpha,\beta))\,\mathrm{d}\alpha\,\mathrm{d}\beta = 0 \tag{2.8}$$

in the case of the method of regularized Stokeslets, where the forces are on the flagellum surface Σ. The discretization of (2.6) with N points results in $3N$ equations for the $3N$ unknown force components. Equation (2.7) (or (2.8)) represent six scalar constraints on the forces, which can be met by introducing six more degrees of freedom: an overall translational velocity $\boldsymbol{U}$ and an overall rotational velocity $\boldsymbol{\Omega}$ of the ring.

2.1.1. *Slender-body framework*

According to the theory in Lighthill (1976), (2.6) evaluated on the centreline is

$$8\pi\boldsymbol{u}(\boldsymbol{X}(s_0)) = 2\boldsymbol{f}_\perp + \int_{r_0>h_0} \frac{\boldsymbol{f}(s)}{r_0} + \frac{(\boldsymbol{f}(s)\cdot\boldsymbol{r}_0)\boldsymbol{r}_0}{r_0^3}\,\mathrm{d}s, \tag{2.9}$$

where $\boldsymbol{r}_0 = \boldsymbol{X}(s) - \boldsymbol{X}(s_0)$, $r_0 = \|\boldsymbol{r}_0\|$ and $\boldsymbol{f}_\perp$ is the component of force perpendicular to the flagellum centreline and is defined by $\boldsymbol{f}_\perp = \boldsymbol{f} - (\boldsymbol{f}\cdot\tau)\tau$ (where $\tau = \boldsymbol{X}'(s)/\|\boldsymbol{X}'(s)\|$ is the unit tangential vector). The integral is along the filament with the portion $[s_0 - h_0, s_0 + h_0]$ removed, where $h_0 = r_h\sqrt{e}/2$ with r_h equal to the dimensionless helical tube radius.

2.1.2. *Regularized Stokeslet framework*

This formulation begins with the Stokes equations $\Delta \boldsymbol{u} = \nabla p - \boldsymbol{F}$, $\nabla \cdot \boldsymbol{u} = 0$, with the surface representation of the forces at an arbitrary point $\boldsymbol{x}$ as

$$\boldsymbol{F}(\boldsymbol{x}) = \iint_{\Sigma} \boldsymbol{f}(\alpha, \beta)\phi_\epsilon(\boldsymbol{x} - \boldsymbol{X}(\alpha, \beta))\,\mathrm{d}\alpha\,\mathrm{d}\beta, \tag{2.10}$$

where $\phi_\epsilon(\boldsymbol{x})$ is a *cutoff function* with the property that $\iiint \phi_\epsilon(\boldsymbol{x})\,\mathrm{d}\boldsymbol{x} = 1$.

Taking the divergence of the Stokes equations in unbounded flows yields $\Delta p = \boldsymbol{f} \cdot \nabla \phi_\epsilon$. We define a regularized Green function G_ϵ as the solution of $\Delta G_\epsilon = \phi_\epsilon$ and the auxiliary function B_ϵ as the solution of $\Delta B_\epsilon = G_\epsilon$. Using these functions, one can write the solution

$$p(\boldsymbol{x}) = \iint_{\Sigma} \boldsymbol{f}(\alpha, \beta)) \cdot \nabla G_\epsilon(\boldsymbol{x} - \boldsymbol{X}(\alpha, \beta))\,\mathrm{d}\alpha\,\mathrm{d}\beta, \tag{2.11}$$

$$\boldsymbol{u}(\boldsymbol{x}) = \iint_{\Sigma} (\boldsymbol{f}(\alpha, \beta) \cdot \nabla)\nabla B_\epsilon(\boldsymbol{x} - \boldsymbol{X}(\alpha, \beta)) - \boldsymbol{f}(\alpha, \beta) G_\epsilon(\boldsymbol{x} - \boldsymbol{X}(\alpha, \beta))\,\mathrm{d}\alpha\,\mathrm{d}\beta. \tag{2.12}$$

The method of regularized Stokeslet is based on the following boundary-integral formulation derived by Cortez *et al.* (2005):

$$\iiint_{\mathbb{R}^3} u_j(\boldsymbol{x})\phi_\epsilon(\boldsymbol{x} - \boldsymbol{X}(\alpha, \beta))\,\mathrm{d}\boldsymbol{x} = \frac{1}{8\pi} \iint_{\Sigma} S_{ij}^{\epsilon}(\boldsymbol{x}, \boldsymbol{X}(\alpha, \beta)) f_i(\alpha, \beta)\,\mathrm{d}\alpha\,\mathrm{d}\beta, \tag{2.13}$$

where S_{ij}^{ϵ} is the expression for a regularized Stokeslet. Using the particular cutoff function of Cortez *et al.* (2005) leads to the following version of (2.6):

$$8\pi \boldsymbol{u}(\boldsymbol{x}) = \iint_{\Sigma} \frac{(r^2 + 2\epsilon^2)\boldsymbol{f}(\alpha, \beta) + (\boldsymbol{f}(\alpha, \beta) \cdot \boldsymbol{r})\boldsymbol{r}}{(r^2 + \epsilon^2)^{3/2}}\,\mathrm{d}\alpha\,\mathrm{d}\beta, \tag{2.14}$$

where $\boldsymbol{r} = \boldsymbol{x} - \boldsymbol{X}(\alpha, \beta)$, $r = \|\boldsymbol{r}\|$, and Σ is the surface of the helical ring. The regularization parameter ϵ is typically chosen of the order of the surface discretization.

2.2. *Dynamic, elastic calculations*

Dynamic simulations of the helical ring using the method of regularized Stokeslets can be computed through the use of an elasticity model that provides the forces on the flagellum from its current geometry, and using those forces to compute the surface velocity through (2.6). We discretize the surface of the helical tube with points along circular cross-sections. Each point is connected by springs to several other nearby points. Each spring is assigned a stiffness constant κ_{Sj} and a resting length δ_j. The simulation is accomplished by dynamically changing the resting lengths of all springs in order to induce a travelling wave along the helix.

Assume that at time $t = t_n$ we know the location of all surface points $\boldsymbol{X}_k$ ($k = 1, 2, \ldots, N_p$) and the resting lengths $\delta_j(t_n)$ ($j = 1, 2, \ldots, N_s$) of all springs. The computation proceeds as follows:

(*a*) For $k = 1, 2, \ldots, N_p$, compute the force density $\boldsymbol{f}_k$ at $\boldsymbol{X}_k$ by

$$\boldsymbol{f}_k = \sum_j \frac{\kappa_{Sj}}{\delta_j(t_n)}(\|\boldsymbol{X}_k - \boldsymbol{X}_{k(j)}\| - \delta_j(t_n))\frac{\boldsymbol{X}_{k(j)} - \boldsymbol{X}_k}{\|\boldsymbol{X}_k - \boldsymbol{X}_{k(j)}\|}, \tag{2.15}$$

where the sum is over all springs that connect $\boldsymbol{X}_k$ to other points $\boldsymbol{X}_{k(j)}$.

(*b*) Given the force density $\boldsymbol{f}_k$, use a discretization of (2.14) to compute the velocities $\boldsymbol{u}(\boldsymbol{X}_k)$ and evolve the particles by $\mathrm{d}\boldsymbol{X}_k/\mathrm{d}t = \boldsymbol{u}(\boldsymbol{X}_k)$ one time step.

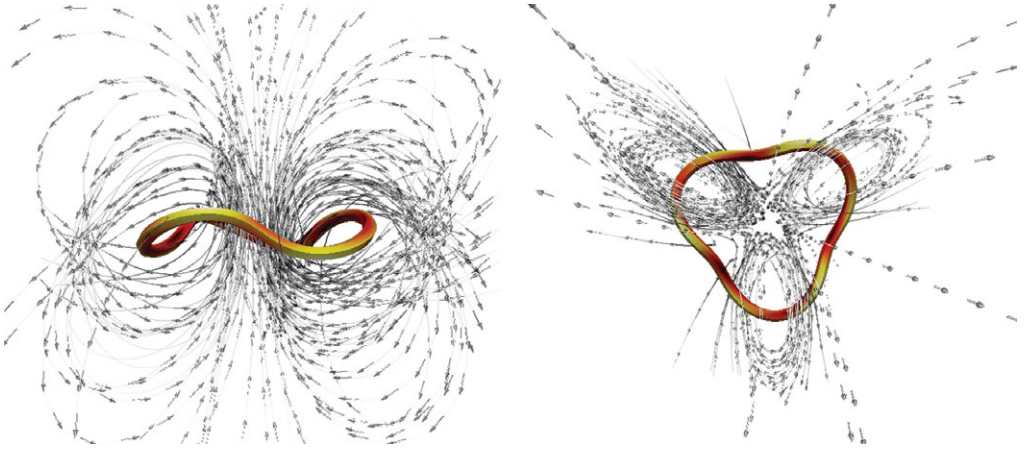

FIGURE 3. (Colour online) Instantaneous three-dimensional streamlines induced by the waving cylindrical ring from different perspectives. The travelling wave is anticlockwise when viewed from above.

We note that since all forces are derived from springs, the net force and net torque are automatically zero. In all computations, we set all dimensionless spring stiffnesses to one. We found these stiffnesses to be large enough so that the emergent waveform was sufficiently close to the desired travelling wave.

3. Numerical results

3.1. *Model problem*

We begin our investigation of the fluid dynamics of waving cylindrical rings by choosing one with three pitches $n_p = 3$ and amplitude $R = 0.09$ (see (2.1)). The cross-sectional radius of the tube is $r_h = 0.035$. Figure 3 shows instantaneous streamlines induced by the waving cylindrical ring, upon which a travelling wave tangential to the ring is imposed. This wave moves anticlockwise when viewed from above. Note that there is significant upward flow in the centre of the ring that results from the motion of each circular cross-section of the ring. Figure 4 shows snapshots of the ring as the wave progresses within a period, along with velocity fields projected onto the xz-plane (figure 4*a*) and the xy-plane (figure 4*b*). Although the ring is periodic, we place a cut in it to demonstrate that there is tangential motion of material points of the ring in the direction opposite of the wave. Even though these snapshots depict a very short time interval, one can also note a slight shift upwards of the ring in the xy-plane as the wave progresses.

The velocity fields shown in figures 3 and 4 were computed using the regularized Stokeslet formulation with dynamic forcing. The ring was discretized using 110 circular cross-sections, with 6 points on each cross-sections ($N_p = 660$). As in Cortez *et al.* (2005), we chose the regularization parameter ϵ to be proportional to the average distance $\hat{\delta}$ between linked points on the discretized surface and found that $\epsilon = (7/12)\hat{\delta}$ gave us the closest agreement between velocities computed using slender-body theory and those computed using the dynamic, elastic calculations. Convergence was demonstrated by computations using finer discretizations of the ring surface and regularization parameter.

It is important to note that the motion of this flexible, cylindrical ring is not a rigid-body rotation. This is in contrast to the rigid rotation of a helical bacterial flagellum about its centreline that generates a torque that must be balanced by the

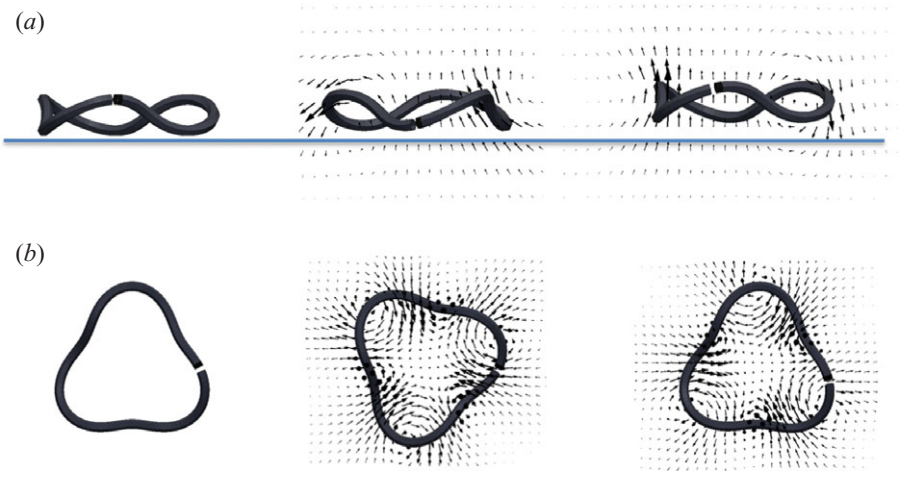

FIGURE 4. (Colour online) Snapshots within one period of ring and velocity fields on (*a*) the *xz*-plane and (*b*) the *xy*-plane of a waving cylindrical ring with three pitches. Time increases from left to right. Note that a cut on the ring is included to demonstrate rotational motion and a horizontal line in (*a*) elucidates translational motion.

FIGURE 5. Snapshots of ring taken 1/2 of a temporal period apart. The material patch on the surface, visible in each frame, demonstrates that the motion is not a rigid-body rotation of the helix about its axis. The force vectors are also depicted along the surface, with the colours indicating magnitude.

rotation of a cell body. Figure 5 shows two snapshots in time of the model ring with a material patch of the surface coloured. These two snapshots are 1/2 of a temporal period apart. If the ring was undergoing a rigid rotation about the helical axis, the coloured patch that is visible in the first frame, would, in the second frame, be facing the interior of the ring and be out-of-view. In fact, the patch is clearly visible in both frames. A supplementary movie, from which the frames of figure 5 were extracted, is available at journals.cambridge.org/flm, so that the reader can easily visualize the dynamics of the waving ring. Since the movie depicts only a short time course of the propagating wave, one cannot detect the net rotational motion of the Lagrangian patch nor its net translational motion. Figure 5 also depicts the force vectors applied at each of the discrete points of the surface. As mentioned above, these forces result from linear springs connecting points on the ring surface, which guarantees that the net force and net torque applied at each instant are zero.

3.2. *Effect of wave amplitude on velocities*

Here, we examine the effect of the dimensionless wave amplitude R on the rotational and translational velocities of the ring. We define the rotational velocity to be the velocity tangential to the circular axis of the ring's helical centreline, and denote

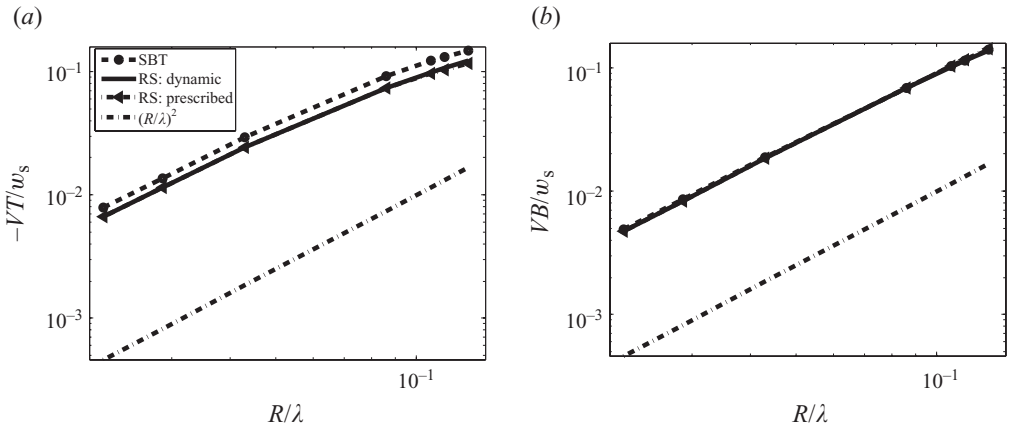

FIGURE 6. Log–log plots of (a) normalized rotational velocity ($-VT/w_s$) versus R/λ and (b) normalized translational velocity (VB/w_s) versus R/λ computed using slender-body theory (SBT), regularized Stokeslets with prescribed wave kinematics (RS: prescribed), and regularized Stokeslets with dynamic forcing (RS: dynamic).

this velocity by VT. Similarly, we define the translational velocity to be the velocity perpendicular to the plane of this circular axis, and denote this velocity as VB. Recall that the classical analysis of Taylor (1952) showed that for small amplitude R a waving cylindrical ring whose axis was straight gave rise to velocities $VT = O(R^2)$ in the direction tangential to the axis. Of course, the order must be even in the amplitude, since the geometry is unchanged when R is replaced by $-R$. Using the same geometric parameters as in the model problem above, we use slender-body theory, regularized Stokeslet calculations with prescribed kinematics and a regularized Stokeslet simulation with dynamic forcing to compute VT and VB for different amplitudes R. We normalize the velocities by the non-dimensional wave speed and the radius by the non-dimensional wavelength. Figure 6 shows a log–log plot of $-VT/w_s$ and VB/w_s versus R/λ. We also plot R^2 for reference. We see that both the rotational and translational velocities exhibit $O(R^2)$ behaviour, with some deviation in the rotational velocity for larger amplitudes R. In comparing the numerical approaches, we see that the calculated VT and VB using Stokeslets with prescribed kinematics or Stokeslets with dynamic forcing are indistinguishable. Both Stokeslet formulations discretize the surface of the cylindrical tube, while slender-body theory relies only on a discretization of the helical centreline. While slender-body theory slightly overestimates the rotational velocity, it captures translational velocities that are also indistinguishable from the Stokeslet formulations. Note that our Stokeslet formulations used a surface discretization as described above, and our slender-body calculations discretize the centreline using 2500 points, with integrals approximated by the trapezoidal rule. In the simulations with dynamic forcing, the velocities reported were computed after a short transient time interval.

3.3. *Effect of number of pitches around ring on velocities*

We examine the effect of varying the number of pitches on a cylindrical ring, with all other geometric parameters fixed (see figure 7 for examples of these geometries). Note that a cylindrical tube with zero pitches around the circle is just a closed torus, and no travelling wave can be imposed. Moreover, since the tube has finite thickness, there is a maximal number of pitches that can actually be realized. As the

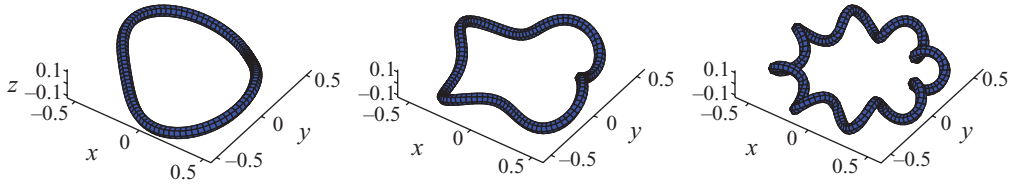

FIGURE 7. Cylindrical rings with 2, 4 and 8 pitches.

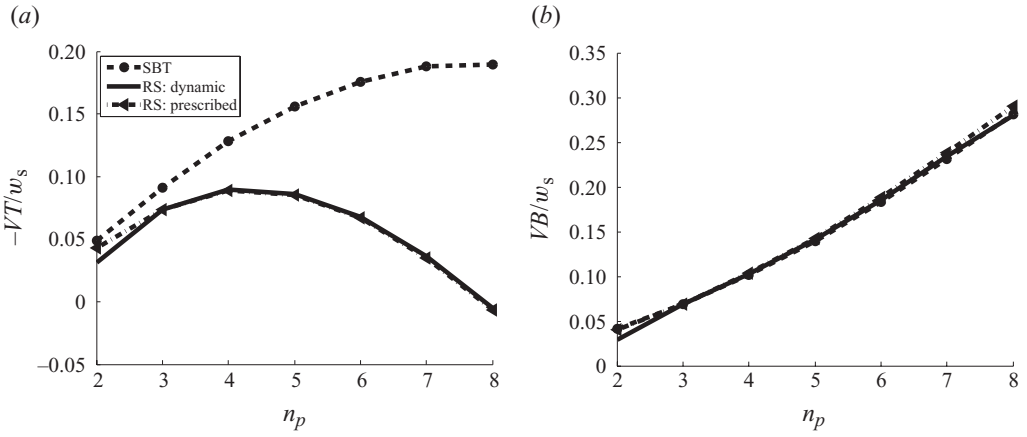

FIGURE 8. (*a*) $-VT/w_s$ versus number of pitches n_p and (*b*) VB/w_s versus n_p computed using using slender-body theory (SBT), regularized Stokeslets with prescribed wave kinematics (RS: prescribed) and regularized Stokeslets with dynamic forcing (RS: dynamic).

number of pitches reaches this maximal values, the profile that the ring presents to the fluid would be nearly that of a torus again, and the propulsion would be inefficient. We expect, therefore, that there will be an optimal number of pitches for a given geometry of the ring that will maximize rotational velocity VT. (This property was also observed for a straight helix by Cortez *et al.* 2005.) However, as will be discussed below, each cross-section of the tube in this extreme case is still undergoing a periodic orbit reminiscent of Purcell's toroidal swimmer (Leshansky & Kenneth 2008) that will result in translational motion. Figure 8 shows plots of the rotational and tangential velocities normalized by the dimensionless wave speed w_s (which depends upon the number of pitches n_p) computed using slender-body theory, regularized Stokeslets with prescribed wave kinematics, and regularized Stokeslets with dynamic forcing. We see that both Stokeslet formulations capture the existence of an optimum pitch for maximizing normalized rotational velocity, but the slender-body theory does not. We also see that the translational velocities increase with the number of pitches and that there is excellent agreement among all three numerical methods in the computation of the translational velocity.

3.4. *Effect of simultaneous change of slenderness and amplitude on velocities*

Here we examine how rotational and translational velocities change as the non-dimensional tube radius and non-dimensional helix amplitude are changed simultaneously. In other words, we choose non-dimensional helix amplitude $R_\beta = \hat{R}/\beta$ and non-dimensional tube radius $r_\beta = \hat{r}/\beta$, with the model problem parameters $\hat{R} = 0.09$ and $\hat{r} = 0.035$, and examine how the velocities depend upon the parameter

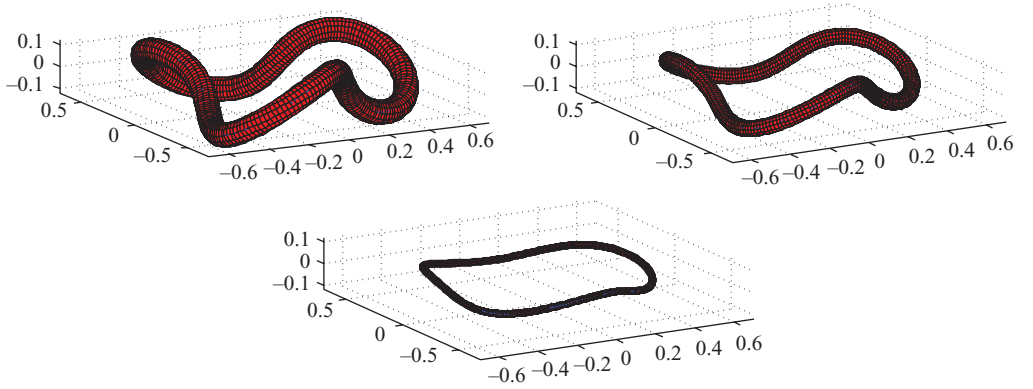

FIGURE 9. (Colour online) Cylindrical rings with three pitches $\beta = 1/3,\ 1/2,\ 5/4$.

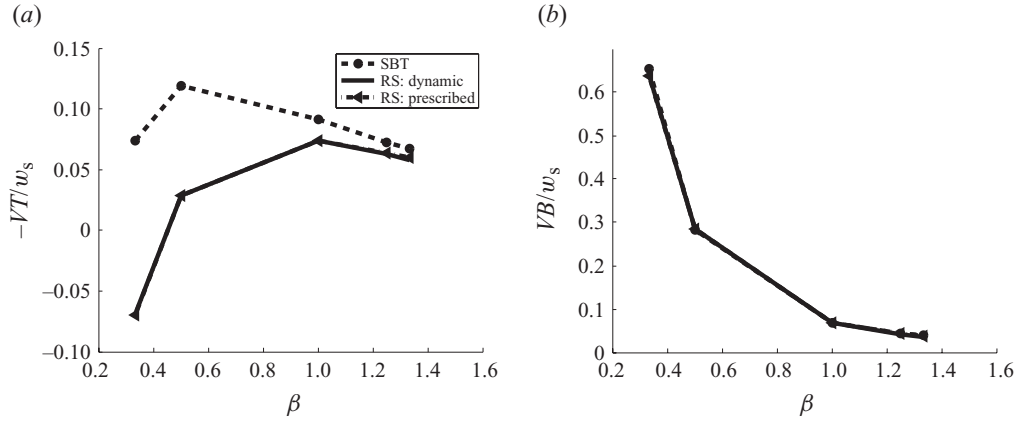

FIGURE 10. (*a*) $-VT/w_s$ versus scaling factor β and (*b*) VB/w_s versus β computed using slender-body theory (SBT), regularized Stokeslets with prescribed wave kinematics (RS: prescribed) and regularized Stokeslets with dynamic forcing (RS: dynamic). Note that as β increases, the tube thickness and the helix amplitude decrease at the same rate.

β. We note that, in dimensional variables, this is analogous to keeping the tube radius and helix amplitude fixed, but varying the radius of the baseline circle. Figure 9 shows examples of these geometries for $\beta = 1/3,\ 1/2$ and $5/4$, respectively. The periodic cylindrical tail analysed by Taylor (1952) swims opposite to the direction of the travelling wave, and by no means exhibits any swimming normal to that direction. The translational velocity of the cylindrical ring, however, arises precisely because of its circular shape and the collective stirring by cross-sections of the ring. Considering the dimensional ring, as the radius of the baseline circle increases, we expect the translational velocity to decrease and the rotational velocity to converge to the swimming velocity of a straight, infinite helix. This behaviour is, indeed, reflected in the calculations presented in figure 10, which shows $-VT/w_s$ and VB/w_s versus β computed using slender-body theory, regularized Stokeslets with prescribed wave kinematics, and regularized Stokeslets with dynamic forcing. Moreover, we see that for the largest helical amplitude and thickest rube, regularized Stokeslet formulations show that the rotational velocity of the ring is in the same direction of the wave. The first frame in figure 9 demonstrates the complexity of

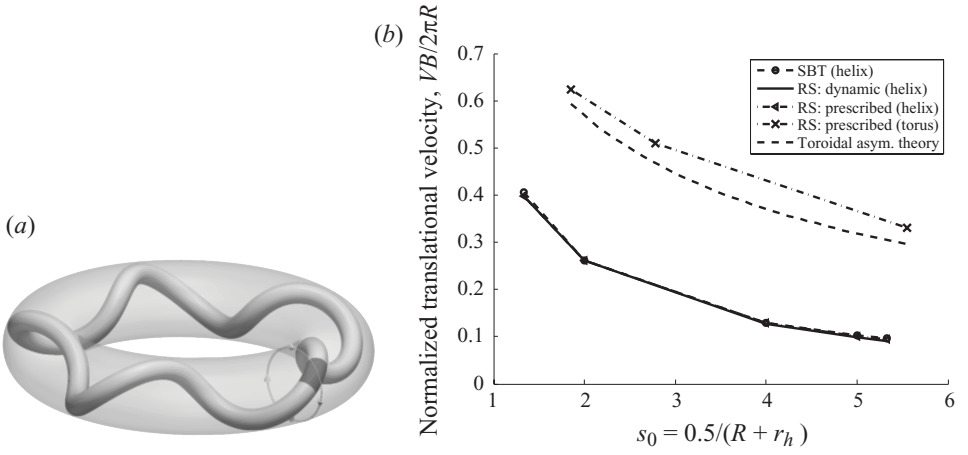

FIGURE 11. (*a*) Visualization of the helical tube inscribed in a torus. (*b*) $VB/2\pi R$ versus s_0 computed for the helical ring. In addition, the scaled translational velocities for the circumscribing torus predicted by the asymptotic (asym.) theory from Leshansky & Kenneth (2008) are shown, along with regularized Stokeslet computations of these toroidal swimming velocities.

the geometry of this case, and gives a visual indication that the assumptions of slender-body theory are not appropriate. However, we see that as the ring geometry meets more closely the assumptions of slender-body theory, the rotational velocities computed using slender-body theory approach those arrived at by the Stokeslet formulations.

3.5. *Comparison with toroidal swimmer*

In both Taylor (1952) and Purcell (1977), a drawing of a hypothetical simple swimmer in the shape of a cylinder wrapped into a torus was presented. Would the twirling of each of the circular cross-sections about the circular torus axis, at constant angular velocity, cause the torus to swim in a Stokes fluid? Recently, Leshansky & Kenneth (2008) analysed this toroidal swimming due to surface rotations and showed that the swimmer is propelled against the direction of its outer surface. For the ratio $s_0 = b/a$, where b is the radius of the circular axis of the torus, a is the cross-section radius, and u_s the surface speed of each cross-section, they compute a translational velocity $V \approx (u_s/2s_0)(\log 8s_0 - (1/2))$ in the limit of large s_0. Figure 11 allows us to visualize the relationship between our waving cylindrical ring and the toroidal swimmer, by inscribing the cylindrical ring in a torus whose radius is $b = 0.5$ and the cross-sectional radius is $a = R + r_h$. For the torus, each point on a circular cross-section rotates with a constant angular velocity. On the other hand, only a segment of the helical tube, while tracing out roughly the same cross-section of the circumscribing torus, contributes an angular velocity. Figure 11 shows the comparison of the computed scaled translational velocity versus the ratio s_0 for the helical ring, along with the asymptotic results for the circumscribing torus in Leshansky & Kenneth (2008). As expected, the translational velocity of the torus is greater than that of the inscribed helical ring. In addition, we computed the translational velocity of the toroidal swimmer using steady Stokeslet calculations, and these values show good agreement with the asymptotic theory (see figure 11).

4. Discussion

In an effort to understand the function of the longitudinal flagellum of dinoflagellates, we have formulated a simple fluid mechanical system of a waving cylindrical ring moving in a Stokes fluid. We conclude that the travelling wave imposed around the ring induces both rotational and translational motions. We have also used this model system to compare regularized Stokeslet formulations with slender-body theory, two popular numerical methods for Stokes flow. When computing rotational velocities of the ring, slender-body theory calculations agree very well with regularized Stokeslet calculations for thinner rings with small helix amplitudes and rings supporting smaller number of helical pitches. In these cases, the assumptions of slender-body theory are more closely met. What is striking is the consistent, close agreement between the two numerical approaches when computing translational velocities. We conjecture that the largest contribution to the rotational velocity at a cross-section comes from the cross-section itself and others nearby. It is a local process. On the other hand, the translational velocity at a cross-section is a result of the far-field flow generated by the portion on the opposite side of the tube. We conclude that the translational velocity is less sensitive to local changes in the geometry than the rotational velocity, allowing slender-body approximations to still give good approximations. We remark that we have chosen not to compute velocities based upon resistive force theory, since it has been shown to give significant errors for helical filaments with appreciable curvature (Jung *et al.* 2007; Yand, Wolgemuth & Huber 2009).

Recently, the method of regularized Stokeslets has been used as a computational framework for modelling low-Reynolds-number flows around cilia and flagella (e.g. Gillies *et al.* 2009; Qian *et al.* 2009; Smith 2009). In the majority of these applications, the flow is induced by prescribing the kinematics of the immersed structure. However, the regularized Stokeslet formulation easily captures the coupling of flexible structure with the surrounding fluid (e.g. Flores *et al.* 2005). In this case, forces due to passive elasticity and active bending moments applied by the immersed structure induce the flow, and the geometry of the structure emerges from the resulting velocity. Here, we have solved the helical ring problem by prescribing kinematics as well as by using an elastic model that achieves the desired kinematics by specifying time-dependent rest lengths of stiff springs connecting points on the surface of the ring. We believe that the simple model problem presented here provides a validation in support of other Stokeslet models with dynamic forcing.

While we have now achieved an understanding of the motion of an isolated waving cylindrical ring, more work remains in analysing the fluid dynamics of dinoflagellate swimming. Future models will include the presence of a cell body and a longitudinal flagellum, along with the study of fluid–dynamic interactions between model dinoflagellates.

The work of H.N. and L.F. was partially funded by the NSF grant NSF-OCE 0724598. The work of R.O. and R.C. was partially funded by the NSF grants DMS-0612625 and EPS-0701491.

REFERENCES

Cachon, M., Cachon, J., Cosson, J., Greuet, C. & Huitorel, P. 1991 Dinoflagellate flagella adopt various conformations in response to different needs. *Biol. Cell* **71**, 175–182.

Cortez, R. 2001 The method of regularized Stokeslets. *SIAM J. Sci. Comput.* **23**, 1204.

Cortez, R., Fauci, L. & Medovikov, A. 2005 The method of regularized Stokeslets in three dimensions: analysis, validation, and application to helical swimming. *Phys. Fluids* **17**, 031504.

Fenchel, T. 2001 How dinoflagellates swim. *Protist* **152**, 329–338.

Flores, H., Lobaton, E., Mendez-Diez, S., Tlupova, S. & Cortez, R. 2005 A study of bacterial flagellar bundling. *Bull. Math. Bio.* **67**, 137–168.

Gaines, G. & Taylor, F. 1985 Form and function of the dinoflagellate transverse flagellum. *J. Protozool.* **32** (2), 290–296.

Gillies, E., Cannon, R., Green, R. & Pacey, A. 2009 Hydrodynamic propulsion of human sperm. *J. Fluid Mech.* **625**, 445–474.

Jung, S., Mareck, K., Fauci, L. & Shelley, M. 2007 Rotational dynamics of a superhelix towed in a Stokes fluid. *Phys. Fluids* **19**, 103105.

Latz, M., Bovard, M., VanDelinder, V., Segre, E., Rohr, J. & Groisman, A. 2008 Bioluminescent response of individual dinoflagellate cells to hydrodynamic stress measured with millisecond resolution in a microfluidic device. *J. Exp. Biol.* **211**, 2865–2875.

Leshansky, A. & Kenneth, O. 2008 Surface tank treading: propulsion of Purcell's toroidal swimmer. *Phys. Fluids* **20**, 063104.

Lighthill, J. L. 1976 Flagellar hydrodynamics. *SIAM Rev.* **18**, 161–230.

Miyasaka, I., Nanba, K., Furuya, K., Nimura, Y. & Azuma, A. 2004 Functional roles of the transverse and longitudinal flagella in the swimming motility of *prorocentrum minimum* (dinophyceae). *J. Exp. Biol.* **207**, 3055–3066.

Purcell, E. M. 1977 Life at low Reynolds numbers. *Am. J. Phys.* **45**, 3–11.

Qian, B., Jiang, H., Gagnon, D., Breuer, K. & Powers, T. 2009 Minimal model for synchronization induced by hydrodynamic interactions. *Phys. Rev.* E **80**, 061919.

Sheng, J., Malkiel, E., Katz, J., Adolf, J., Belas, R. & Place, A. 2007 Digital holographic microscopy reveals prey-induced changes in swimming behavior of predatory dinoflagellates. *Proc. Natl Acad. Sci.* **104** (44), 17512–17517.

Smith, D. J. 2009 A boundary element regularized Stokeslet method applied to cilia-and flagella-driven flow. *Proc. R. Soc. Lond.* A **465**, 3605–3626.

Taylor, G. I. 1952 The action of waving cylindrical tails in propelling microscopic organisms. *Proc. R. Soc. Lond.* A **211**, 225–239.

Yand, J., Wolgemuth, C. & Huber, G. 2009 Kinematics of the swimming of *spiroplasma*. *Phys. Rev. Lett.* **102**, 218102.